

cuVSLAM: CUDA accelerated visual odometry and mapping

Alexander Korovko¹, Dmitry Slepichev¹, Alexander Efitorov¹, Aigul Dzhumamuratova¹, Viktor Kuznetsov¹, Joydeep Biswas¹, Hesam Rabeti¹ and Soha Pouya¹

¹NVIDIA, {akorovko, dslepichev, aefitorov, adzhumamuratova, vkuznetsov, jbiswas, hrabeti, spouya}@nvidia.com

Abstract

Accurate and robust pose estimation is a key requirement for any autonomous robot. We present cuVSLAM, a state-of-the-art solution for visual simultaneous localization and mapping, which can operate with a variety of visual-inertial sensor suites, including multiple RGB and depth cameras, and inertial measurement units. cuVSLAM supports operation with as few as one RGB camera to as many as 32 cameras, in arbitrary geometric configurations, thus supporting a wide range of robotic setups. cuVSLAM is specifically optimized using CUDA to deploy in real-time applications with minimal computational overhead on edge-computing devices such as the NVIDIA Jetson. We present the design and implementation of cuVSLAM, example use cases, and empirical results on several state-of-the-art benchmarks demonstrating the best-in-class performance of cuVSLAM.

Acknowledgements

We would like to extend our heartfelt acknowledgment to Eugene Vendrovskiy, Stanislav Volodarskiy, and Dmitry Robustov for their invaluable contributions to this project. Their profound expertise, exceptional skills, and commitment to excellence have been pivotal in shaping the outcomes of this work.

1. Introduction

Visual Simultaneous Localization and Mapping (VSLAM) is a fundamental capability for autonomous robots, enabling them to build a metric map of their environment while simultaneously determining their location within it. The increasing deployment of autonomous robots across diverse applications, from warehouse automation to last-mile delivery, has created a pressing need for robust, real-time VSLAM solutions that can operate efficiently across diverse settings, while being able to run on energy-efficient edge computing devices.

Traditional VSLAM systems face several key challenges: they often struggle with real-time performance on resource-constrained platforms, have limited flexibility in sensor configurations, and may not fully utilize available hardware acceleration capabilities. Additionally, many existing solutions are optimized for specific sensor configurations, making them less adaptable to diverse robotic platforms with varying sensor requirements.

We present cuVSLAM, a CUDA-accelerated visual SLAM system designed to address these challenges. cuVSLAM offers several key innovations:

- Flexible sensor suite support, accommodating configurations from a single RGB camera to complex arrays of up to 32 cameras with arbitrary geometric arrangements
- Support for optional IMU and depth sensors
- Efficient CUDA implementation enabling real-time performance on edge devices like NVIDIA Jetson
- A modular architecture separating frontend pose estimation from backend map refinement
- Robust feature tracking and mapping capabilities that maintain accuracy across diverse environments

Our technical approach combines classical SLAM techniques with modern GPU acceleration. The frontend module performs real-time pose estimation using feature detection, tracking, and local mapping, while the backend handles global map consistency through pose graph optimization and loop closure. By leveraging CUDA acceleration throughout the pipeline, from feature detection to bundle adjustment, cuVSLAM achieves superior performance while maintaining high accuracy.

We evaluate cuVSLAM on standard benchmarks including KITTI, EuRoC, and TUM RGB-D, demonstrating state-of-the-art accuracy while maintaining real-time performance on edge computing platforms. Our results show that cuVSLAM achieves average trajectory errors below 1% on the KITTI odometry benchmark and mean position errors under 5cm on the EuRoC dataset, while processing frames in real-time on NVIDIA Jetson platforms.

The rest of this technical report is organized as follows: Section 2 describes the system architecture and design, Section 3 presents experimental results and benchmarks, and Section 4 concludes with discussion and future work.

2. System Architecture and Design

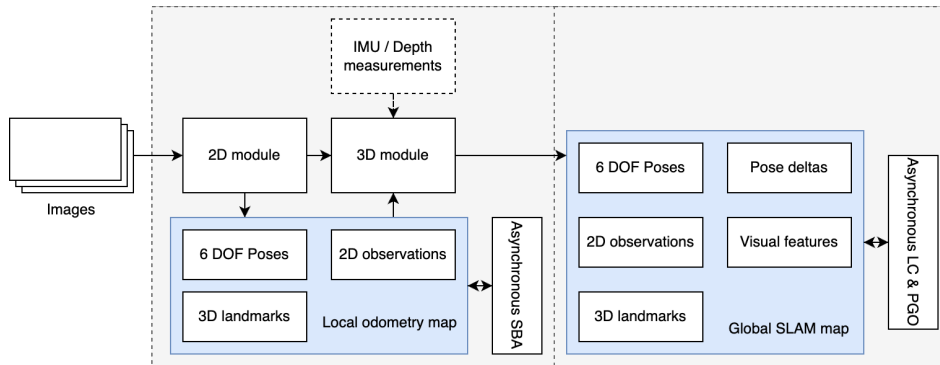


Figure 1: cuVSLAM architecture

The cuVSLAM library implements a general approach to camera pose estimation, where the architecture consists of two major blocks: the frontend, responsible for online pose estimation with minimal latency and maximum throughput, and the backend, focusing on asynchronous and potentially resource-demanding map refinement, loop closing, and pose graph optimization.

The design of the frontend pipeline prioritizes local pose estimation accuracy over global consistency, focusing on delivering smooth trajectories without the bumps introduced by loop closure mechanisms or PGO (Pose Graph Optimization). To achieve this, it maintains a local odometry map consisting of the last N 6DOF camera poses (at keyframes) along with visible 3D landmarks and their observations. Besides the map, the frontend consists of the 2D module, responsible for feature selection, 2D feature tracking, and keyframe selection, and the 3D module, which performs pose estimation based on the local map, 2D information, and other data sources (e.g., IMU or depth measurements).

In contrast to the frontend, cuVSLAM’s backend focuses on global map and pose consistency. It processes frontend outputs and builds a globally consistent map that integrates camera poses, 2D observations, 3D landmarks, pose deltas, and visual features. The backend maintains global consistency in the map through asynchronous refinement using pose graph optimization and loop closing.

2.1. 2D module

cuVSLAM implements a set of algorithms operating on the 2D level, which include keypoint selection and feature extraction, keypoint tracking, and keyframe selection.

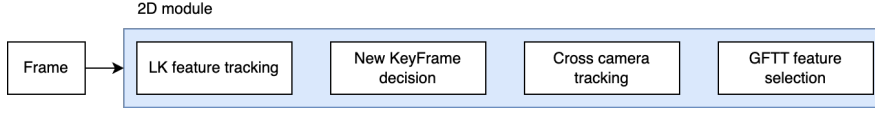


Figure 2: 2D module implements keyframe selection, feature selection and 2D tracking.

The pipeline begins with keypoint selection, which is designed to identify high-contrast features and ensure an approximately uniform distribution of keypoints across the image. The image is first divided into non-overlapping patches, forming an $N \times M$ grid. In each patch, the algorithm selects the top k keypoints based on the "Good Features to Track" measure (Shi and Tomasi (1993)), where k is calculated such that the total number of keypoints across the entire image exceeds a predefined threshold, K_I .

$$k > \left\lceil \frac{K_I}{N * M} \right\rceil \quad (1)$$

For 2D tracking, cuVSLAM implements a modified version of the Lucas-Kanade algorithm (Lucas and Kanade (1981), Bouguet (2000)) for feature tracking that: 1) performs tracking in a coarse-to-fine manner, continuously refining track positions at each image pyramid level, and 2) performs a normalized cross-correlation (NCC) check at each optimization step for each keypoint to filter out unreliable tracks.

If the number of successfully tracked keypoints falls below a threshold, the 2D module creates a new keyframe, which triggers local and global map updates and asynchronous refinement. In stereo and multicamera modes, cuVSLAM launches cross-camera feature tracking to obtain multi-view observations for subsequent landmark triangulation.

2.2. 3D module

When a keyframe is created, the 3D module collects multi-view observations from the 2D module and performs landmark triangulation. The created landmarks, along with their observations, are saved in the local map. After pose estimation, an asynchronous local sparse bundle adjustment (SBA) is initiated for refinement. Given the poses T_i , landmarks p_j , and 2D observations o_{ij} , SBA solves the following optimization task:

$$r_{ijk}^{repr} = \pi(T_k^{cb} T_i^{bw} p_j^w) - o_{j,k} \quad (2)$$

$$\hat{T}_{1:N}^{bw}, \hat{p}_{1:M}^w = \arg_{T_{1:N}^{bw}, p_{1:M}^w} \min \sum_{i \in [1, N]} \sum_{j \in [1, M]} \sum_{k \in [1, C]} \|\pi(T_k^{cb} T_i^{bw} p_j^w) - o_{j,k}\|_{\Sigma}^2 \quad (3)$$

where r^{repr} represents reprojection error, T_k^{cb} refers to the k -th camera-from-base transformation, T_i^{bw} denotes the base-from-world transformation, p_j^w is the 3D landmark in the world frame, and $o_{j,k}$ represents the observation of landmark j by the k -th camera.

Following the common approach, we use the Schur complement to solve for poses T_i first and solve for points p_j afterward. To enhance the efficiency of SBA further, we implement it in CUDA, which is particularly useful for edge devices and/or in multicamera setups. cuVSLAM supports mono, stereo, multicamera, and visual-inertial modes, each of which corresponds to a dedicated 3D solver.

2.2.1. Stereo

Stereo mode is the default mode in cuVSLAM. It utilizes PnP algorithm for pose estimation, that relies on o_j , 2D observation, and p_i , 3D landmarks, acquired from the local map.

$$\hat{T}^{bw} = \arg_{T^{bw}} \min \sum_{j \in [1, M]} \sum_{k \in [1, 2]} \|r_{jk}^{repr}\|_{\Sigma}^2 \quad (4)$$

On regular frames, we perform tracking only for the left camera for the tracks that are still active. We query the local map for the corresponding 3D landmarks and use them for pose estimation. When the number of successfully tracked keypoints falls below a threshold, a keyframe is created. After feature selection, we perform cross-camera (left-to-right) tracking to obtain landmark stereo observations and conduct point triangulation. Finally, we add the current camera pose, along with the created landmarks and their observations, into the local map and launch asynchronous SBA for refinement.

2.2.2. Multicamera

When a robot operates in environments where it is likely to face a featureless surface from one direction, e.g., narrow corridors or elevators, it becomes vital to use multiple cameras for pose estimation.

cuVSLAM extends the approach introduced in 2.2.1 to a multicamera setup by treating an arbitrary multiple-camera configuration as a number of stereo pairs.

At startup, we build a Frustum Intersection Graph (FIG)—a directed graph (V, E) , where vertices V represent a set of optical sensors, and edges E connect cameras that share a common field of view. Edge direction describes the cross-camera tracking between adjacent cameras, i.e., if e_{ij} exists, cuVSLAM performs 2D tracking from camera c_i to c_j .

The FIG is built automatically at cuVSLAM’s startup. Provided with a list of camera extrinsics/intrinsics, cuVSLAM iterates over each pair of cameras and creates a new edge in the graph when cameras have overlapping fields of view (FoV). To detect this, cuVSLAM places a virtual plane in front of the first camera. It selects uniformly distributed pixels in the image I_1 , lifts them onto the plane, and backprojects them to the image I_2 . When the ratio of successfully projected points to the total number of sampled points exceeds a threshold, cuVSLAM detects the shared FoV and creates an edge.

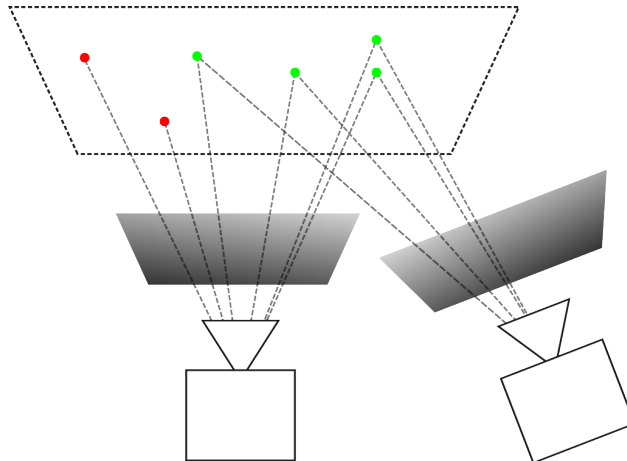


Figure 3: Randomly selected pixels on left picture are lifted on a virtual plane in front of the camera. Pixels that can be successfully projected onto second images are shown in green.

Cameras that correspond to the source of some edge are used for feature tracking/selection over time on each incoming frame. A keyframe is still treated as a global event, while feature selection happens independently

for each camera.

Let S_{curr} be a set of all currently observed points from all the cameras and S_{kf} is the set of points observed in the previous keyframe. Then if:

$$\frac{|S_{curr} \cap S_{kf}|}{|S_{kf}|} < T; \quad (5)$$

a keyframe is created and cross-camera tracking is done. Similar to stereo mode we then perform landmark triangulation and refine the map with SBA.

After 2D tracking both on regular frames and keyframes, we collect all the available observations along with the corresponding 3D landmarks for pose estimation.

$$\hat{T}^{bw} = \arg_{T^{bw}} \min \sum_{j \in [1, M]} \sum_{k \in [1, C]} \|r_{jk}^{repr}\|_{\Sigma}^2 \quad (6)$$

where r^{repr} denotes a reprojection error for j -th landmark observed from k -th camera in the rig [Barfoot \(2017\)](#).

Since observations from multiple cameras contribute to pose estimation, cuVSLAM requires images to be synchronized. This is a minor restriction, as many modern cameras provide hardware synchronization capabilities, such as Intel RealSense ?.

2.2.3. Visual-Inertial

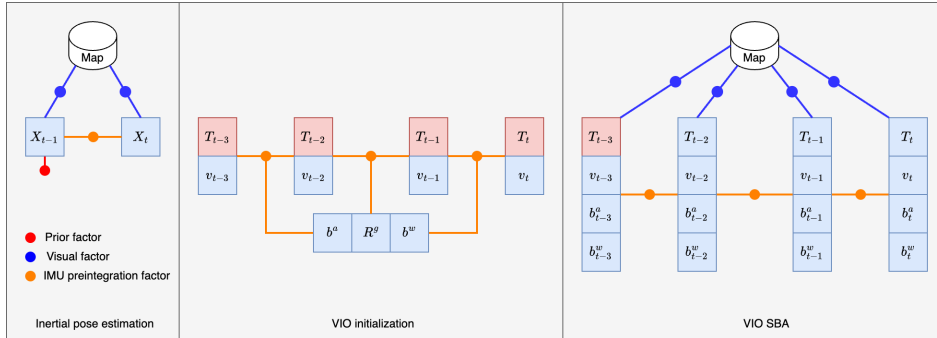


Figure 4: Factor graphs for VIO pipeline.

Visual-Inertial (VI) mode is inspired by [Forster et al. \(2017\)](#) and [Campos et al. \(2021\)](#). Following their approach cuVSLAM defines robot's state as a combination of 6 DoF pose, linear velocity, accelerometer and gyroscope biases forming a 15 DoF state vector $S = [T \in SE(3), v \in \mathbb{R}^3, b^a \in \mathbb{R}^3, b^w \in \mathbb{R}^3]$. Robot states along with IMU (r^{imu}) and visual (r^{repr}) factors are used to build a factor-graph for a list of crucial subproblems, which are:

- *Purely visual pose estimation* is used for the initialization of VI pipeline. It consists of the PnP and the asynchronous SBA as it was described in section 2.2.1 and needed to build a pose history for the subsequent gravity estimation.
- *Gravity estimation*. Gravity is a key parameter needed for the IMU preintegration and IMU-aided pose estimation. Assuming the poses predicted by the visual-only part are fixed, the algorithm estimates velocities v_i , accelerometer and gyroscope biases b^a , b^w and a rotation matrix R^g , s.t. $g = R^g[0, 0, 9.81]^T$.

$$R^g, \mathbf{b}, v_{0:k} = \operatorname{argmin} \left[\|b\|_{\Sigma_{prior}}^2 + \sum_{i=0}^{k-1} \|r^{imu}(S_i, S_{i+1})\|_{\Sigma_{IMU}}^2 \right] \quad (7)$$

- *Visual-inertial pose estimation* is used every frame. It constrains two consecutive robot states S_{i-1} and S_i with IMU and visual factors. In addition S_{i-1} is also constrained by the prior factor.

$$S_{i-1}, S_i = \underset{\text{argmin}}{\left[\left\| r^{imu}(S_{i-1}, S_i) \right\|_{\Sigma_{IMU}}^2 + \sum_{j=0}^1 \left\| r^{repr}(S_{i-j}) \right\|_{\Sigma_{vis}}^2 + \left\| r^{prior}(S_{i-1}) \right\|_{\Sigma_p}^2 \right]} \quad (8)$$

- *Visual-inertial sparse bundle adjustment* is used for local map refinement when IMU data along with gravity and bias estimations are available. Following prior works, we perform relinearization of the IMU factors based on the variable update norm or once per number of iterations.

$$S_{0:k} = \underset{\text{argmin}}{\left[\sum_{i=1}^k \left\| r^{imu}(S_{i-1}, S_i) \right\|_{\Sigma_{IMU}}^2 + \sum_{i=0}^k \left\| r^{repr}(S_i) \right\|_{\Sigma_{vis}}^2 \right]} \quad (9)$$

2.2.4. RGBD

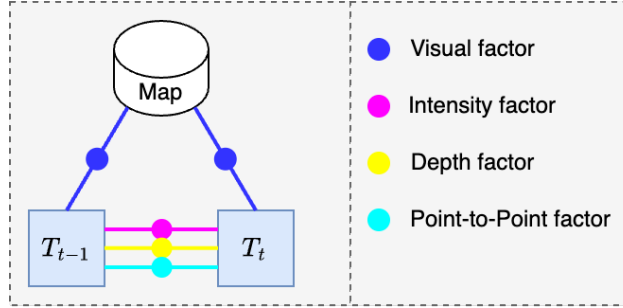


Figure 5: RGBD factor graph.

cuVSLAM supports mono RGBD-based dense frame-to-frame pose estimation. Following [Kerl et al. \(2013\)](#) it considers two consecutive intensity images $I_{1,2}$ along with pixel-aligned depth images $Z_{1,2}$ and estimates a relative 6 DoF transformation between corresponding frames.

It defines a list of factors, that constrain frame positions w.r.t each other:

- **Visual factor** used to constrain poses w.r.t the local map by means of reprojection error r^{repr} described earlier.
- **Dense intensity and depth factors** define constraints for each pixel location x , introducing the following error functions:

$$r^I = \begin{bmatrix} I_2(\tau(T_{21}, x)) - I_1 \\ I_1(\tau(T_{21}^{-1}, x)) - I_2 \end{bmatrix} \quad (10)$$

$$r^Z = \begin{bmatrix} Z_2(\tau(T_{21}, x)) - [T_{21}\pi^{-1}(x, Z_1(x))]_z \\ Z_1(\tau(T_{21}^{-1}, x)) - [T_{21}^{-1}\pi^{-1}(x, Z_2(x))]_z \end{bmatrix} \quad (11)$$

where T_{21} is the relative pose; $\tau(T, x)$ is a warping function, that lifts the pixel location x to 3D, applies transformation T and projects the point back to image plane; $[\cdot]_z$ returns Z coordinate of a point.

- **Point-to-point factor.** Provided with the 2D-2D matches $(x, y)_{1:N}$ obtained in 2D module, we define the point-to-point error:

$$r^p = \pi^{-1}(y, Z_2(y)) - T_{21}\pi^{-1}(x, Z_1(x)) \quad (12)$$

All together these factors form the combined optimization problem, which we solve using a Levenberg-Marquardt

solver implemented on GPU:

$$\hat{T}_{21} = \arg_{T_{21}} \min \left(\sum_{p \in \text{Points}} \|r^{repr}(p)\|_{\Sigma}^2 + \sum_{x \in \text{Pixels}} (\|r^I(x)\|^2 + \|r^Z(x)\|_{\sigma_z}^2) + \sum_{(x,y) \in \text{Tracks}} \|r^p(x,y)\|^2 \right) \quad (13)$$

2.2.5. Mono

Mono camera mode shares the same common approach as 2D feature tracking, with subsequent point triangulation and pose estimation. A key difference is that triangulation is performed using observations obtained from different camera poses, which we estimate using the same PnP algorithm as described in 2.2.1, given the current observations of previously obtained landmarks.

For the first frame pair, when no 3D landmarks are available, cuVSLAM estimates the relative transformation through the fundamental matrix. Specifically, given a set of 2D tracks $(x, y)_{1:N}$, we estimate the fundamental matrix F using RANSAC. With the calibration matrix K , we then retrieve the up-to-scale relative pose.

The relative pose is subsequently used to triangulate the first set of landmarks and update the local map, followed by asynchronous SBA refinement.

2.3. Loop closing and global map refinement

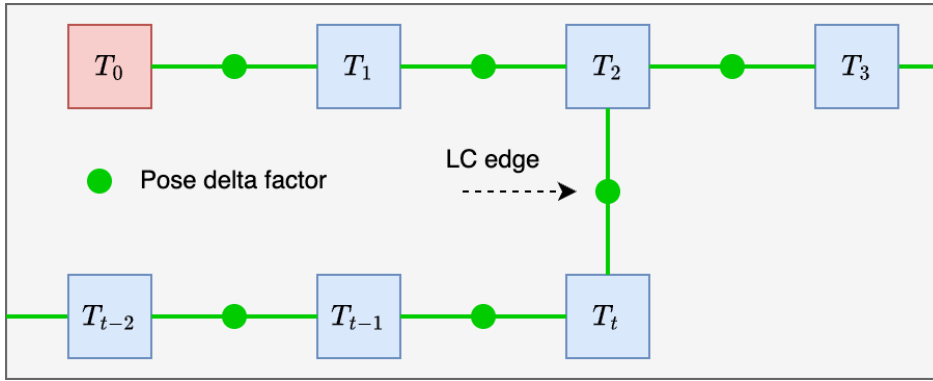


Figure 6: Factor graphs for VIO pipeline.

cuVSLAM’s loop closing and global map refinement module helps limit global drift by enforcing global consistency of the map. It consists of 6 DoF keyframe poses, landmarks and their observations, pose deltas, and sparse image features. Pose deltas are obtained through the integration of intra-keyframe frontend pose predictions. For image features, we use a list of 9×9 image patches taken from each level of the image pyramid.

We perform the following steps to detect loop closures and refine the map to enforce global consistency:

- **Integrate latest data.** When a new keyframe is created, cuVSLAM extracts visual features, integrates intra-keyframe pose predictions, collects currently visible landmarks along with their observations and updates the global map using an asynchronous data queue.
- **Query nearest neighbors.** After the map update, cuVSLAM performs a pose search of robot poses within a sphere of fixed radius. We use a kd-tree for fast and efficient spatial search.
- **Landmark selection.** After collecting all the landmarks related to the found poses, we: 1) filter them by geometric visibility, 2) track landmark visual features onto the currently observed image, and 3) filter out landmarks with unsuccessful tracking. Finally, when landmarks from multiple poses are observed, we split the landmarks into sets with respect to connected poses and pick the largest set.
- **Relative pose estimation.** At this step, we estimate a pose delta D between the pose from the map and the current robot’s position. Let T^{mw} denote a pose in the map, connecting the *world* and *map* frames.

Then, after shifting landmarks into the *map* frame, we solve for the relative pose estimate:

$$\hat{T}^{bm} = \arg_{T^{bm}} \min \sum_{j \in [1, M]} \sum_{k \in [1, C]} \|\pi(T_k^{cb} T^{bm} T^{mw} p_j^w) - o_{j,k}\|_{\Sigma}^2 \quad (14)$$

- **Pose graph optimization.** Provided with the pose deltas between poses either by the frontend or the loop closure mechanism, cuVSLAM refines the map by minimizing the following sum across pose graph edges E :

$$T_{1:N} = \arg_{T_{1:N}} \min \sum_{i,j \in E} \|\text{Log}(D_{ij}^{-1} T_i^{-1} T_j)\|^2 \quad (15)$$

3. Experiments

This section demonstrates the capabilities of the cuVSLAM library in robotics applications across diverse real-world environments and camera configurations. We also compare our solution with established classical and deep learning libraries that provide camera pose estimation for long-distance trajectories.

3.1. System Performance and Hardware Utilization

We evaluated cuVSLAM’s performance in real-time live execution to measure embedded hardware utilization, as well as using recordings from a warehouse environment to measure visual tracking execution time on embedded and workstation hardware. During these experiments, cuVSLAM processed feature-rich images captured either from a wheeled robot or from handheld camera movements, representing typical usage scenarios.

Table 1: cuVSLAM Performance Evaluation. The left side shows per-call processing times measured on RTX4090 (Desktop) and Orin AGX 64gb (Jetson), all images in datasets have 768×480 resolution (except mono-depth mode with resolution 640×480). The right side summarizes hardware utilization (CPU and GPU) measured on the Jetson platform running cuVSLAM via the Python API with live RealSense cameras at 640×480 resolution and 30 FPS

Configuration	Track call time, ms		Jetson HW utilization	
	Desktop	Jetson	CPU %	GPU %
Mono	0.9	2.7	NA	NA
Mono-Depth	5.9	13.9	2.4	45.0
Stereo	0.4	2.7	0.4	1.7
Stereo-Inertial	1.3	3.8		
Multicamera (2-stereo)	0.8	2.7	1.1	5.9
Multicamera (3-stereo)	1.4	2.8	1.5	7.1
Multicamera (4-stereo)	2.1	2.8	NA	NA

The left side of [Tab. 1](#) summarizes execution times for the cuVSLAM visual tracking function, excluding image acquisition and result post-processing overhead. Performance was measured on two hardware configurations: a desktop workstation equipped with an Intel i7-14700 CPU and NVIDIA RTX 4090 GPU, and an embedded single-board Jetson Orin AGX 64GB platform running in MAXN power mode.

The right side of [Tab. 1](#) presents CPU and GPU utilization percentages for cuVSLAM visual odometry executed through the Python API with RealSense D435/D455 cameras running at 30 FPS. These measurements were conducted live, in real-time. To isolate cuVSLAM’s hardware resource requirements, we performed two controlled experiments: first, we measured baseline system utilization with the RealSense camera in motion but without cuVSLAM processing input data; then, we repeated the identical camera movement pattern with cuVSLAM visual tracking enabled. Resource utilization metrics were sampled at 15 ms intervals for identical durations in both experiments. cuVSLAM’s net resource consumption was calculated by subtracting baseline measurements from total utilization and averaging the results. This approach accurately reflects the additional computational overhead introduced by the library. Note that these measurements were performed in

a controlled environment, excluding other resource-intensive operations such as visualization, complex image processing, or data recording, which could otherwise skew results by overloading the system.

3.2. Benchmarking

Table 2: Evaluation results for cuVSLAM Visual Odometry and SLAM across various operating modes

Mode	Dataset	Method	ATE, %	ARE, deg	APE (RMSE)
Mono-Depth	ICL-Nuim	ORB_SLAM3	-	-	-
		DPVO	10.28	0.77	0.61
		cuVSLAM Odom	0.41	0.99	0.026
		cuVSLAM SLAM	0.44	0.97	0.026
	TUM RGB-D	ORB_SLAM3	0.50	2.98	0.067
		DPVO	13.56	1.98	0.80
		cuVSLAM Odom	1.35	5.52	0.11
		cuVSLAM SLAM	0.99	4.13	0.065
Stereo	EuroC*	ORB_SLAM3	0.21	1.41	0.068
		DPVO	0.21	0.96	0.10
		cuVSLAM Odom	0.29	1.96	0.13
		cuVSLAM SLAM	0.17	1.12	0.054
	Kitti	ORB_SLAM3	0.31	1.20	2.98
		DPVO	21.69	1.14	195.05
		cuVSLAM Odom	0.33	1.14	3.00
		cuVSLAM SLAM	0.27	0.93	1.98
	TartanAir	ORB_SLAM3	-	-	-
		DPVO	12.73	0.79	12.84
		cuVSLAM Odom	0.44	1.78	0.44
		cuVSLAM SLAM	0.49	1.85	0.50
Stereo-Inertial	EuroC	ORB_SLAM3	5.70	72.23	0.066
		DPVO	-	-	-
		cuVSLAM Odom	0.39	2.69	0.19
		cuVSLAM SLAM	0.29	2.27	0.13
Multi-Stereo	R2B	ORB_SLAM3	-	-	-
		DPVO	5.35	0.81	12.30
		cuVSLAM Odom	0.18	1.15	0.28
		cuVSLAM SLAM	0.11	0.70	0.18

The cuVSLAM operation modes were evaluated using several publicly available datasets: Mono-Depth mode was validated on the ICL-NUIM [1] and TUM RGB-D [2] datasets; Stereo mode was tested on the EuroC [3], KITTI [4], and TartanAir [5] datasets; and Stereo-Inertial mode was assessed using the EuroC dataset. Standard metrics were employed to quantify the accuracy of the estimated trajectories: Average Relative Translation and Rotation Errors proposed in [6], as well as Absolute Pose Error with trajectory alignment and scale correction [7] using the EVO library [8].

To ensure accurate and representative comparisons, clearly identified outlier sequences were excluded. For instance, the EuroC V203 sequence was included only in Stereo-Inertial evaluations, and certain sequences from the TartanAir and TUM RGB-D datasets were omitted. A complete list of the sequences used from each dataset is provided in Appendix A.

To rigorously validate cuVSLAM’s multi-camera capabilities, we collected a proprietary Multi-Stereo R2B dataset from office and warehouse environments using the Nova Carter wheeled robot equipped with four stereo cameras. Example scenes are shown in Fig. 7, and trajectories are illustrated in Fig. 10. A detailed description of this dataset is presented in Appendix B. Ground truth trajectories for these evaluations were obtained using high-precision lidar localization.

The use of a proprietary dataset was necessary because cuVSLAM’s multi-camera mode requires images captured by hardware-synchronized cameras, which could be combined in multiple stereo pairs. Currently, publicly available multi-camera datasets generally lack either hardware-synchronized cameras suitable for stereo pair arrangements ?, ? or employ software synchronization that does not ensure simultaneous image capture ?, ?.

We anticipate that recent growth in availability and adoption of synchronized multi-stereo camera systems from various vendors will encourage creation of new public multi-camera datasets, facilitating further development, testing, and implementation of multi-camera SLAM systems in robotic applications.

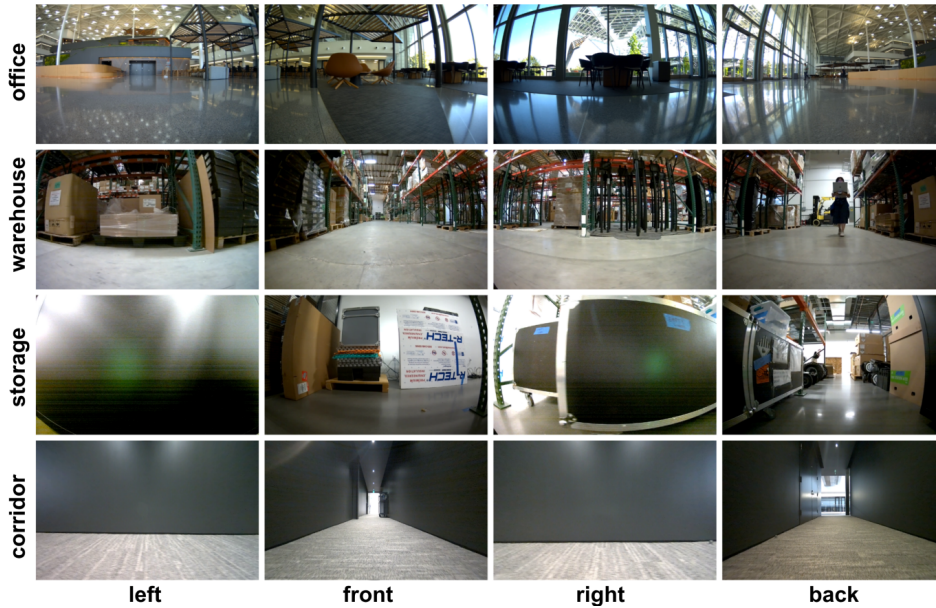


Figure 7: Sample camera views from the R2B dataset captured across diverse environments including large office spaces, industrial warehouses, and narrow corridors in both office and storage areas. The images show simultaneous captures from 4 stereo cameras (displaying only the left image from each stereo pair) taken by the Carter Robot

Tab. 2 presents comprehensive benchmarking results across popular datasets from various domains. For comparative analysis, we include performance metrics for the classical computer vision-based ORB-SLAM3 and the deep learning-based DPVO alongside cuVSLAM. Each library was configured appropriately for the dataset domain: ORB-SLAM3 and cuVSLAM operated in their corresponding specialized modes (monocular-depth, stereo, or inertial), while DPVO was consistently used in monocular mode across all evaluations (utilizing the front left camera for stereo and multi-camera datasets).

4. Discussion

cuVSLAM demonstrates robust performance across diverse robotic platforms, including automotive vehicles, aerial drones, wheeled robots, and handheld camera setups. Our evaluation covers both real-world and synthetic datasets, providing a comprehensive assessment of the system’s capabilities under varied operational conditions.

The presented results reflect cuVSLAM’s out-of-the-box performance without parameter fine-tuning, relying solely on standard sensor calibration parameters and stable image acquisition. This approach enables successful operation with various camera types and leaves room for potential improvements by end users. For example, in our TUM-RGBD dataset evaluation, raw depth data were used without any preprocessing, despite known limitations in depth quality for this dataset.

4.1. Hardware Scalability and Implementation

cuVSLAM exhibits excellent scalability across hardware platforms and provides effective integration through user-friendly ROS2¹ and Python² APIs. Although this paper primarily considers scenarios involving multiple USB-connected RealSense cameras operating at 30 FPS, the measured visual tracking execution times and hardware utilization indicate significant potential for more demanding configurations. This is confirmed by practical experience, as cuVSLAM has been successfully deployed to process 8 Full HD distorted RGB images at 30 FPS from 4 stereo cameras in real-time on a Jetson Orin AGX as part of the ISAAC Perceptor framework³, which simultaneously runs other resource-intensive components, such as NVBLOX[?] and Nav2[?].

4.2. Advantages and Research Directions

We advocate for wider adoption of multi-camera visual tracking in robotics based on two principal observed advantages: enhanced trajectory reliability in feature-poor environments in odometry mode, and increased loop closure detection rates in SLAM mode. Fig. 8 demonstrates trajectory reliability through a practical test conducted using a Carter robot equipped with four stereo cameras. In this experiment, the robot moved continuously while its cameras were randomly covered with non-transparent film for intervals of 20–60 seconds, ensuring at least one stereo pair remained uncovered at given time. Despite these challenging conditions, the odometry trajectory remained stable without jumps or discontinuities, validating the system’s robustness to partial visual obstruction.

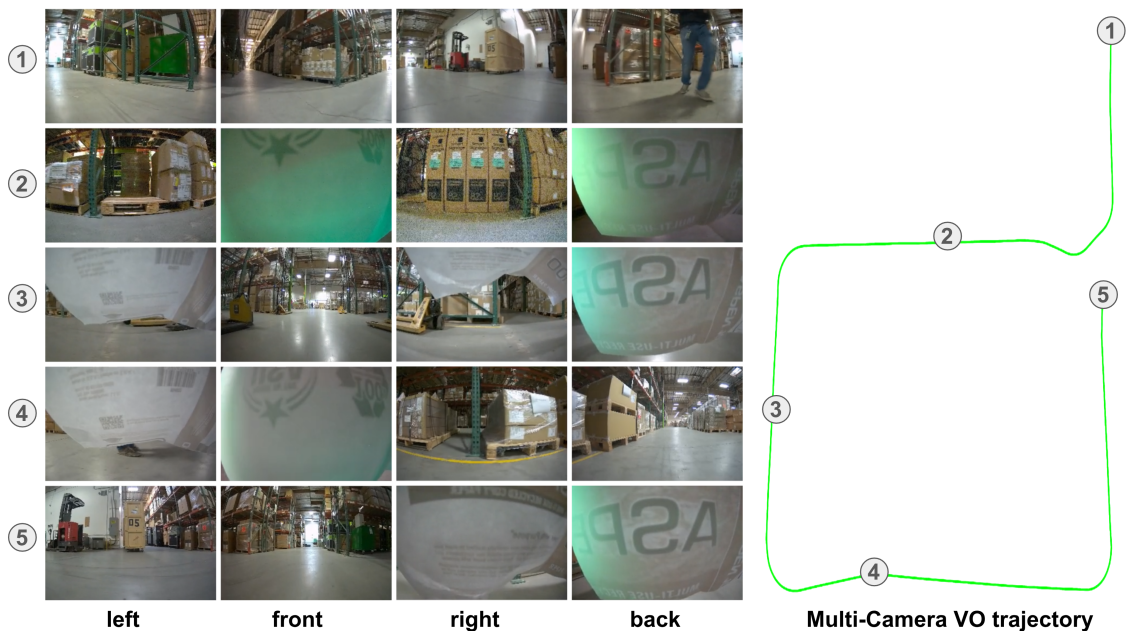


Figure 8: Occlusion resilience test results using the Carter robot. The figure shows the continuous trajectory successfully maintained by cuVSLAM multicamera visual odometry despite random camera occlusions using non-transparent film. Numbered image rows correspond to instantaneous views from the robot’s four stereo cameras (showing only the left image from each stereo pair) at the respective numbered locations along the trajectory.

Additionally, the increased loop closure detection rate resulting from an expanded collective field of view is demonstrated in Fig. 9, comparing the number of loop closure events between single-stereo and four-stereo camera setups for the same trajectory. This higher frequency of camera pose adjustments yields a quantitative improvement of approximately 40% in SLAM accuracy metrics compared to odometry mode, as demonstrated

¹https://github.com/NVIDIA-ISAAC-ROS/isaac_ros_visual_slam

²<https://github.com/NVlabs/PyCuVSLAM>

³<https://developer.nvidia.com/isaac/perceptor>

in Tab. 2 using the Multi-Stereo R2B dataset.

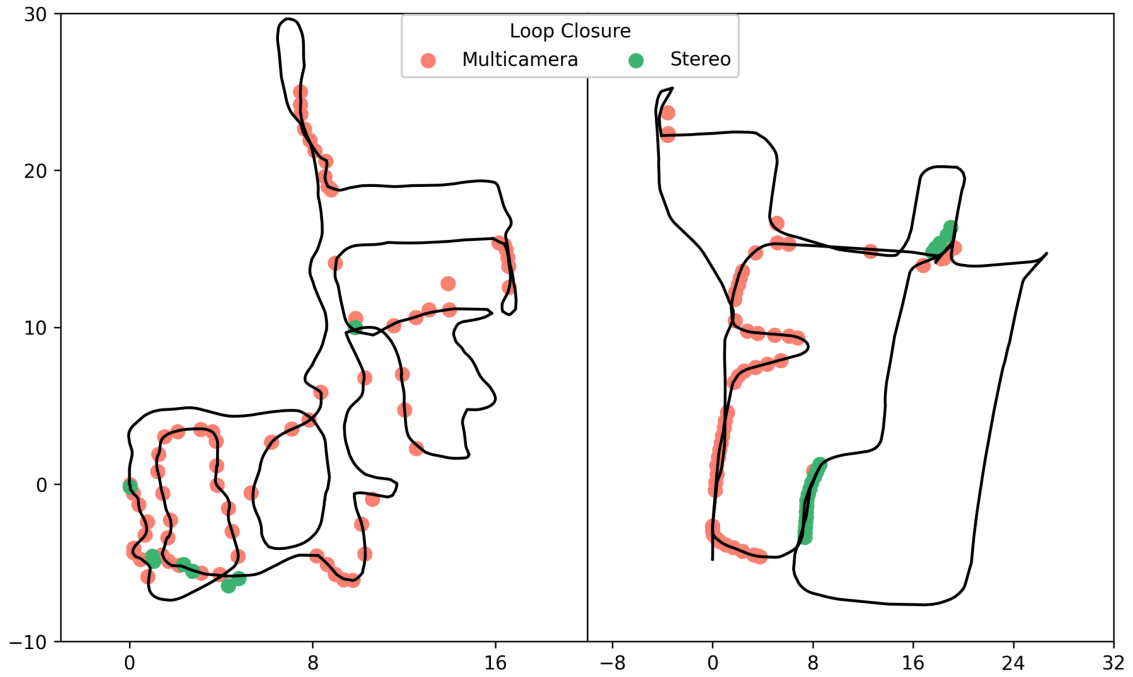


Figure 9: Comparison of loop closure detection events between single-camera and multi-camera (four stereo pairs) SLAM configurations on identical trajectories. The multi-camera setup demonstrates improved mapping consistency due to its wider cumulative field-of-view.

References

- [1] Timothy Barfoot. *State Estimation for Robotics*. 08 2017. ISBN 9781107159396. doi: 10.1017/9781316671528. 5
- [2] J. Y. Bouguet. Pyramidal implementation of the affine lucas kanade feature tracker description of the algorithm. *Microprocessor Research Labs*, 2000. URL https://robots.stanford.edu/cs223b04/algo_tracking.pdf. 3
- [3] Carlos Campos, Richard Elvira, Juan J. Gomez Rodriguez, Jose M. M. Montiel, and Juan D. Tardos. Orbslam3: An accurate open-source library for visual, visual–inertial, and multimap slam. *IEEE Transactions on Robotics*, 37(6):1874–1890, December 2021. ISSN 1941-0468. doi: 10.1109/tro.2021.3075644. URL <http://dx.doi.org/10.1109/TR0.2021.3075644>. 5
- [4] Christian Forster, Luca Carlone, Frank Dellaert, and Davide Scaramuzza. On-manifold preintegration for real-time visual–inertial odometry. *IEEE Transactions on Robotics*, 33(1):1–21, February 2017. ISSN 1941-0468. doi: 10.1109/tro.2016.2597321. URL <http://dx.doi.org/10.1109/TR0.2016.2597321>. 5
- [5] Christian Kerl, Jürgen Sturm, and Daniel Cremers. Dense visual slam for rgb-d cameras. pages 2100–2106, 2013. doi: 10.1109/IROS.2013.6696650. 6
- [6] B. D. Lucas and T. Kanade. An iterative image registration technique with an application to stereo vision. *Proceedings of Imaging Understanding Workshop*, 1981. URL https://www.ri.cmu.edu/pub_files/pub3/lucas_bruce_d_1981_1/lucas_bruce_d_1981_1.pdf. 3
- [7] Jianbo Shi and Carlo Tomasi. Good features to track. *1994 Proceedings of IEEE Conference on Computer Vision and Pattern Recognition*, 37(6), December 1993. ISSN 1063-6919. doi: 10.1109/CVPR.1994.323794. URL <https://ieeexplore.ieee.org/document/323794>. 3

A. Appendix

A.1. Appendix A

The following publicly available datasets were used for validating the libraries:

The TartanAir dataset includes 120 Hard sequences, the complete list is provided in [Tab. 3](#). From the TUM RGB-D SLAM dataset, only the sequences from the freiburg3 subset were utilized, as these sequences specifically provide rectified images required by the cuVSLAM Mono-Depth mode. The 10 sequences employed from this subset are listed in [Tab. 4](#).

Table 3: TartanAir dataset sequences used for evaluation

Environment	Sequences
abandonedfactory	P000-P011
amusement	P000-P007
carwelding	P000-P003
endofworld	P000-P002, P005-P006
hospital	P037-P039, P042, P044-P049
japanesalley	P000-P005
neighborhood	P000-P002, P004, P006-P010, P012-P017
ocean	P000-P008
office2	P000-P002, P004-P008, P010
office	P000, P001, P004, P006
oldtown	P000-P008
seasidetown	P000, P002, P004
seasonsforest	P001-P002, P004-P006
seasonsforest_winter	P010-P018
soulcity	P000-P002, P004, P008, P009
westerndesert	P000, P002, P003, P005-P007

Table 4: TUM RGB-D SLAM dataset sequences used for evaluation

Sequences
large cabinet validation
long office household
nostructure texture far
nostructure texture near withloop
sitting halfsphere
sitting xyz
sitting xyz validation
structure texture far
structure texture near
teddy

A.2. Appendix B

The Multi-Stereo R2B dataset was collected using a wheeled Carter robot equipped with four Full HD RGB stereo Hawk cameras operating at 30 FPS. Stereo cameras are hardware-synchronized, with a maximum synchronization time difference of approximately 0.1 ms within each 8-image batch. Each recording has been validated for completeness regarding lost image batches; the maximum loss rate of image batches is below 0.04%. Fig. 10 shows the trajectories of all sequences along with detailed statistics, including the trajectory distance and the number of synchronized image batches for each recording.

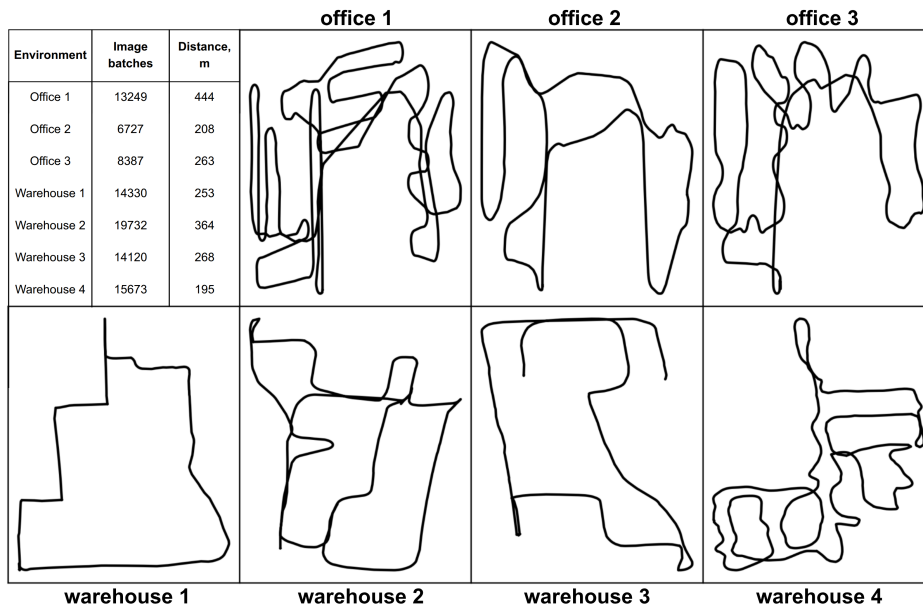


Figure 10: Trajectories of sequences from the Multi-Stereo R2B dataset, along with corresponding distances and the number of 8-image batches per trajectory